A cloud-based 3D BEM framework for predicting the diffusion coefficient

Peter D'Antonio, Luiz Augusto Ferraz Alvim, Rinaldi Petrolli, et al.

ARTICLES YOU MAY BE INTERESTED IN

182nd Meeting of the Acoustical Society of America

Denver, Colorado

23-27 May 2022

Architectural Acoustics: Paper 3aAA7

A cloud-based 3D BEM framework for predicting the diffusion coefficient

Peter D'Antonio
REDI Acoustics, Highland, NY, 12528, USA; dr.peter.dantonio@gmail.com

Luiz Augusto Ferraz Alvim
UFSM: Universidade Federal de Santa Maria, Santa Maria, RS, BRAZIL; luiz.alvim@eac.ufsm.br

Rinaldi Petrolli
REDI Acoustics, LLC Highland, NY, USA; rinaldi.petrolli@rediacoustics.com

Eric Brandão and Paulo Mareze
UFSM: Universidade Federal de Santa Maria, Santa Maria, RS, BRAZIL; eric.brandao@eac.ufsm.br; paulo.mareze@eac.ufsm.br

The experimental measurement of the diffusion coefficient according to ISO 17497-2 is very time-consuming and requires several sample periods to evaluate the effect of diffraction lobes, an anechoic or large reflection-free volume, and far-field conditions. Wave-based BEM methods have predicted the diffusion coefficient very accurately [Hargreaves, T, Cox, T.J., Lam, YW, D'Antonio, P., (2000), "Surface diffusion coefficients for room acoustics: Free-field measures, "J. Acoust. Soc. Am. 108 (4), 1710-1720]. This work will describe a new 3D BEM, cloud-based Python Virtual Goniometer program called VIRGO, which predicts the free-field diffusion coefficient from 3D CAD files. The program accurately predicts the properties of a reference 1-dimensional hemicylinder and periodic diffraction grating lobes from a 2-dimensional hemisphere. Furthermore, 3-dimensional polar responses and normalized diffusion coefficient of additional number-theoretic and optimized profiled and curvilinear shapes will also be compared with scale model boundary-plane goniometer measurements. The results will verify that it is possible to predict the diffusion coefficients following ISO 17497-2 in reasonable time frames without having to fabricate or 3D print scale models or full-scale samples.

1. INTRODUCTION

The characterization of the diffuse reflection properties of surfaces is essential in the fields of architectural and room acoustics. A figure of merit is necessary to allow efficient design and attribute performance specifications to acoustic diffusors. The diffusion coefficient is a standardized metric that evaluates the degree of spatial uniformity of the scattered pressure from a diffusor.[1] It enables comparison between the effectiveness of different products.

In light of the challenges posed by the experimental procedure described in ISO 17497-2[2], numerical simulations are often a viable option to obtain the scattered sound pressure and the diffusion coefficient. Frequency-domain methods are the most common and have dominated the field of diffusor design.[3,4] Remarkable accuracy is achieved with the Boundary Element Method (BEM). Acousticians can conceive arbitrary 3D geometry and predict its diffusion coefficient without needing expensive infrastructure associated with the experimental apparatus. However, it comes at the cost of slow computational times, especially for higher frequencies. The current work aims to solve some of the traditional limitations associated with the method by employing a modern cloud cluster to compute the problem efficiently.

This work intends to present and validate a computer simulation framework to accurately predict the diffusion coefficient and 2D and 3D behavior of diffusive surfaces. The theory involved in predicting the diffusion coefficient and the setup of the 2D and 3D acoustical goniometers are described in Section 2. Section 3 presents the fundamental mathematics for the BEM, remarks on the implementation, and the measurement setups used to acquire the experimental data. Section 4 shows results and discussion on the diffusion coefficient. Polar responses are shown to compare simulation and experimental data, and the normalized diffusion coefficient is analyzed.

2. THE DIFFUSION COEFFICIENT

Two criteria exist to assess a diffusor's performance: the diffusion and the scattering coefficients. While this paper focuses on the diffusion coefficient, described in ISO 17497-2[2], it is essential to clarify the difference between them. The diffusion coefficient, d, measures the uniformity of the scattered sound pressure at different incidence angles on a scale from 0 to 1. The scattering coefficient, s, measures the ratio between the energy diffracted in non-specular directions to the total energy reflected by a sample.[5] The latter is extensively used in geometrical room acoustic simulations, but does not describe the spatial properties of the scattered sound field.

As Hargreaves *et al.*[1] have demonstrated, the diffusion coefficient can be calculated from the autocorrelation function. Using this definition, it is possible to calculate a non-normalized diffusion coefficient for every elevation, θ, and azimuth, ϕ, angle of incidence, with:

$$d_{\theta,\phi} = \frac{\left(\sum\limits_{i=1}^{n} 10^{L_i/10}\right)^2 - \sum\limits_{i=1}^{n} \left(10^{L_i/10}\right)^2}{(n-1)\sum\limits_{i=1}^{n} \left(10^{L_i/10}\right)^2} \tag{1}$$

where L_i is the Sound Pressure Level (SPL) of the one-third octave band scattered pressure measured by the i-th microphone; n is the total amount of measurement points.

The sample acts as a point source at low frequencies, uniformly reflecting energy in all directions. Thus, edge diffraction increases the diffusion coefficient with decreasing frequency. The normalization procedure is applied to factor out the effects of the finite sample. To do so, a reference flat sample with the same overall size as the diffusor must also have its diffusion coefficient measured. To guarantee the reference sample has the same edge profile as the diffusor, the diffusor sample is rotated 180 degrees to expose its flat back to the

sound source. The normalized diffusion coefficient d_n, given by Eq. (2), takes into account only the surface scattering, and better illustrates the frequency at which the diffusor becomes effective.

$$d_n(\theta, \phi) = \frac{d(\theta, \phi) - d_r(\theta, \phi)}{1 - d_r(\theta, \phi)},\qquad(2)$$

in which d_r is the diffusion coefficient of the reference reflector (rotated sample). The coordinate system, as described in ISO 17497-2[2], is shown in Fig. 1a. The random incidence diffusion coefficient is given by averaging the computed angles of incidence according to weights described by ISO 17497-2[2].

(a) Coordinate system.   (b) 2D Goniometer.   (c) 3D Goniometer.
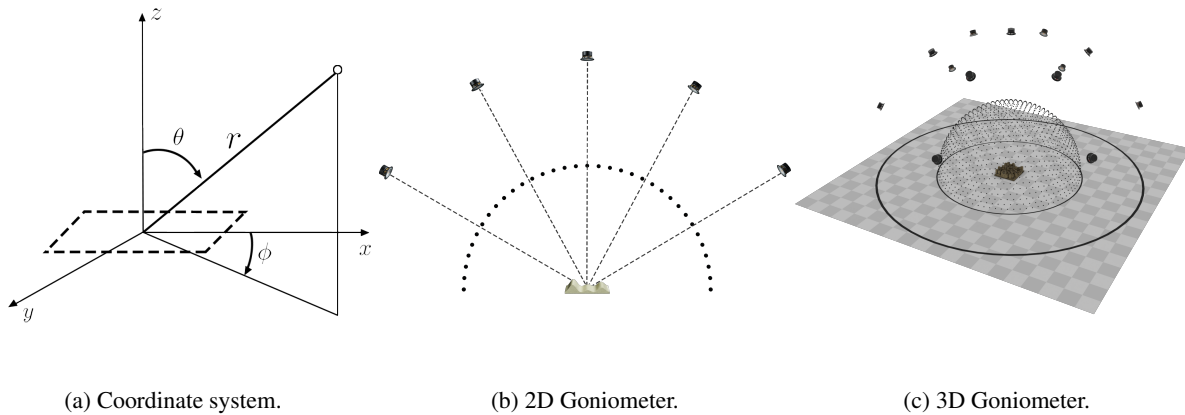
Figure 1: Coordinate system for the diffusion coefficient evaluation with source and receiver positions for 2D and 3D goniometers. The black dots represent receivers and the speaker model, the sources. The checkered plane is for illustration purposes and is not included in the computation.

The standard describes two available measurement techniques, a 2D and 3D setup. The 2D goniometer consists of boundary plane measurements, where sources, receivers, and test samples are placed in the same $xy-$plane, as shown in Fig. 1b. Given the 2D nature, this setup is sufficient to evaluate the behavior of extruded shapes, such as 1D QRD diffusors, hemicylinders, etc. In reality, this can be measured in a large room, with adequate post-processing to remove the room reflections and isolate the response from the test samples, thus creating a virtual anechoic response. The adequate measurement setup, and its limitations, are described in ISO 17497-2[2].

An anechoic room is required to carry out this experiment in 3D, as shown in Fig. 1c. It is a very complex and time-consuming measurement due to the large number of source and receiver combinations required for good spatial resolution. This limitation exists because the reflections of a non-anechoic environment cannot be efficiently windowed during post-processing, given the complex configuration of sources and receivers. On the other hand, the added complexity allows the evaluation of acoustical devices with complex topologies that are not limited to 1D diffusors.

3.   METHODOLOGY

This section introduces the tested samples, the Boundary Element Method (BEM) used in this research, and the experimental setup used to validate the numerical simulations.

A. TEST SAMPLES

The test samples shown in Fig. 2 are proposed to evaluate the validity and performance of the simulations. In Fig. 2, all of the proposed test samples are shown: (2a) 1x1 Hemisphere, (2b) 2x2 Hemispheres, (2c) 4x1 Hemispheres, (2d) 1x1 Hemicylinder, (2e) RPG Modffusor, and (2f) RPG Waveform Bicubic G.

At first, the $30\,\text{cm}$ radius hemicylinder was simulated (Fig. 2d), and the results were compared with experimental measurements. Evaluating the scattering from hemispheres is proposed to observe the 3D capabilities of the framework. Hemispheres were chosen because the diffusion coefficient will exhibit similar behavior to the hemicylinder. In addition, it will also display periodicity effects in 3D when more than one unit is evaluated. The angle of the lobes in the polar responses can be verified analytically for different hemisphere arrangements (Figs. 2a, 2b and 2c).

(a)   (b)   (c)

(d)   (e)   (f)
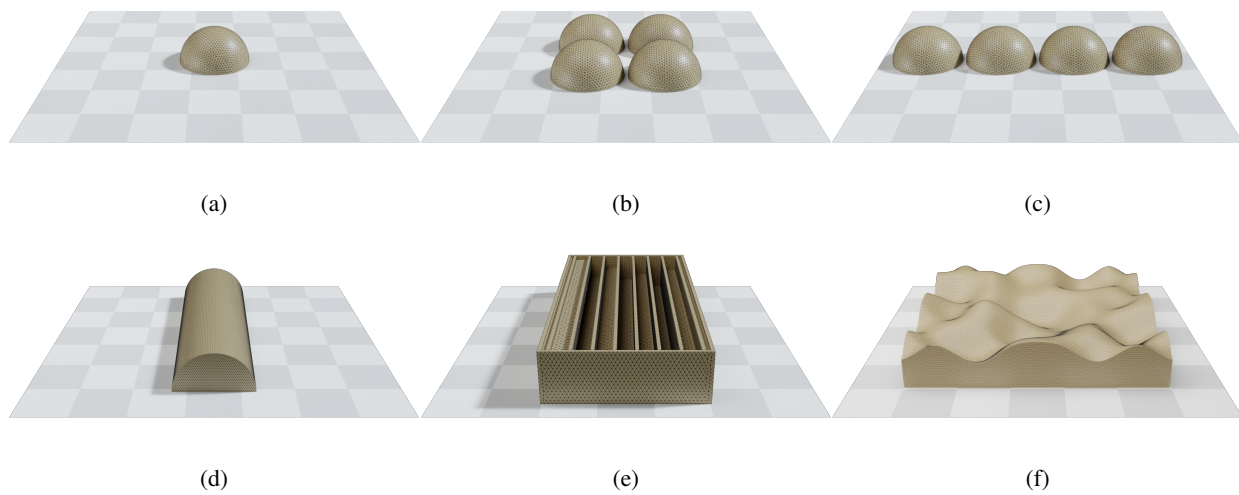
Figure 2: Hemicylinder, hemisphere, and RPG Acoustical System's products meshes of the different studied configurations. The checkered plane is for illustration purposes and is not included in the computation.

In addition, two commercial diffusive products with complex topologies will be evaluated. The Modffusor, Fig. 2e, and the Waveform Bicubic G, Fig. 2f, diffusors from RPG Acoustical Systems were selected.

To mesh the samples, Gmsh[6] was used. Separate meshes for different parts of the frequency spectra are used throughout the simulations to improve computational efficiency. The total number of meshes can be optimized for each case depending on the frequency range of analysis and the characteristics of the sample. The element size is set as $\lambda/6$, with the wavelength denoted as λ.

B. BOUNDARY ELEMENT METHOD

This section presents the boundary integral equations (BIE) implemented to solve the 3D Helmholtz equation for exterior domains. Additionally, a brief description of the implementation is provided.

Consider a closed surface S and let Ω_+ be its exterior domain in $\mathbb{R}^3$. A weak integral formulation using the Green's function, given by Eq. (3), with an impedance boundary condition, leads to Eq. (4).

$$G_k(\vec{r}, \vec{r_s}) = \frac{\mathrm{e}^{-\mathrm{j}k|\vec{r}-\vec{r_s}|}}{4\pi|\vec{r}-\vec{r_s}|} \ , \tag{3}$$

$$c(\vec{r})p(\vec{r}) = p_\mathrm{i}(\vec{r}) + \int_S p(\vec{r_s})\left[\frac{\partial G_k(\vec{r}, \vec{r_s})}{\partial n(\vec{r_s})} - \mathrm{j}k\,\beta(\vec{r_s})\,G_k(\vec{r}, \vec{r_s})\right]\mathrm{d}S \ , \tag{4}$$

with

$$\frac{\partial G_k\left(\vec{r},\vec{r_s}\right)}{\partial n\left(\vec{r_s}\right)} = n \cdot \left[-\frac{(\vec{r}-\vec{r_s})\,\mathrm{e}^{-\mathrm{j}k|\vec{r}-\vec{r_s}|}}{4\pi|\vec{r}-\vec{r_s}|}\left(\mathrm{j}k + \frac{1}{|\vec{r}-\vec{r_s}|}\right)\right] , \tag{5}$$

in which $k = \omega/c_0$ is the wave number in the exterior domain; ω is the angular frequency; n is the normal vector; $\vec{r_s}$ is the coordinate at the surface of the diffuser; $\vec{r}$ is the coordinate of a receptor point, which can be either at the surface of the modelled geometry, when solving for the surface pressure, $p\left(\vec{r_s}\right)$, or at the exterior domain, when calculating field point pressure, $p(\vec{r})$. Furthermore, $c(\vec{r})$ is the leading coefficient, referred as the solid angle of the mesh, given by Eq. (6). Note that for this case, Green's function takes the wave number $k = 0$, leading to the double-layer potential operator of the Laplace problem. For smooth surfaces, $c(\vec{r}) = \frac{1}{2}$ is usually considered, although for the current paper the integration is always computed regardless of the sample. Thus,

$$c(\vec{r}) = \begin{cases} c(\vec{r}) = 1 & \text{if } \vec{r} \text{ is outside } \Omega_- \\ c(\vec{r}) = 0 & \text{if } \vec{r} \text{ is inside } \Omega_- \\ c(\vec{r}) = 1 + \int_S \frac{\partial G_0(\vec{r},\vec{r_s})}{\partial n(\vec{r_s})} dS & \text{if } \vec{r} \in \partial\Omega \end{cases} . \tag{6}$$

A surface impedance Z_s can be attributed to the boundary as the normalized admittance, defined by $\beta\left(\vec{r_s}\right) = \frac{\rho_0 c_0}{Z_s\left(\vec{r_s}\right)}$. This strategy is used to account for locally reactive sound absorption at the surface of the sample. ρ_0 and c_0 are the density and speed of sound in air (or exterior domain), respectively.

Eq. (4) allows the calculation of the total pressure field $p(\vec{r})$ from the scattering of the incident pressure field p_i, generated by a single point source or by a set of sound sources. In 3D space, the point source is given by Green's function as in Eq. (7), where $\vec{r_0}$ denotes the source coordinates.

$$p_\mathrm{i}(\vec{r},\vec{r_0}) = \frac{\mathrm{e}^{-\mathrm{j}k|\vec{r}-\vec{r_0}|}}{4\pi|\vec{r}-\vec{r_0}|} . \tag{7}$$

To solve Eq. (4), the surface S is discretized into linear continuous triangular elements. This constitutes a boundary mesh, such as the ones shown in Fig. 2. A finite sum can approximate the integral equation, where three integration points are used for every element. The resulting system is presented in its matrix form by Eq. (8), where $\mathbf{H}_k$ and $\mathbf{G}_k$ are the dense complex matrices related to Eqs. (3) and (5). The linear system in Eq. (9) is solved with LU Factorization, resulting in the total boundary pressure $\mathbf{p}$.

$$\mathbf{A} = \mathbf{CI} - \mathbf{H}_k - \mathrm{j}k\beta(\vec{r_s})\mathbf{G}_k, \tag{8}$$

$$\mathbf{Ap} = \mathbf{p}_\mathrm{i}. \tag{9}$$

The literature has thoroughly discussed that Eq. (4) breaks down at the eigenvalues corresponding to the interior Dirichlet problem. The current work uses the Combined Helmholtz Integral Equation Formulations (CHIEF) to address this issue.[7] With increasing frequency, more points are selected in the interior domain. The original matrix $\mathbf{H}_k$ is concatenated along its first axis with the corresponding matrix computed for the CHIEF points. The system is solved in the least-squares sense, given by Eq. (10):

$$\mathbf{p} = \left(\mathbf{H}^H\mathbf{H}\right)^{-1}\mathbf{H}^H\mathrm{j}k\beta(\vec{r_s})\mathbf{G}_k , \tag{10}$$

with the superscript ^{H} denoting Hermitian, i.e. the transpose conjugate complex matrix. Details of the implementation are described by Marburg.[7] Having said that, the authors recognize that Burton-Miller[8] is a more robust approach, as demonstrated by Marburg[9] and noted in Section 5.

After the surface quantities are solved with the discretized form of Eq. (4), the boundary pressure can be used to evaluate the complex acoustic pressure at any given field point in the exterior domain. In this case, the leading coefficient is $c(\vec{r}) = 1$. The scattered pressure at receiver coordinates in its matrix form is given by Eq. (11).

$$p_{\mathrm{s}}(\vec{r}) = -\mathbf{H}_k \mathbf{p}_{\mathrm{s}} + jk \, \beta(\vec{r}_s) \mathbf{G}_k \mathbf{p}_{\mathrm{s}}, \ \ \vec{r} \in \Omega_+ \,. \tag{11}$$

$$L_i = 20\mathrm{log}_{10} \left(\frac{\sqrt{\frac{1}{2} p_{\mathrm{s}} p_{\mathrm{s}}^*}}{2 \cdot 10^{-5}} \right) \,. \tag{12}$$

At last, the computed complex scattered pressure p_{s} can be converted to SPL with Eq. (12), where the symbol $*$ indicates the complex conjugate. L_i is the input for calculating the diffusion coefficient. More details on the BEM formulation can be found at Refs.[10, 11]

i.   Implementation Details

The recent advancements in cloud computing allowed a modern implementation of the 3D BEM formulation in Python with the open-source package Dask.[12] Since a broad range of frequencies is desired to evaluate the diffusion coefficient, a parallel implementation is necessary to achieve convenient run times. On top of that, the friction-less scaling provided by the cloud approach enables large problems to be solved, and hence computations of higher frequencies are achieved.

For the problem at hand, the main advantage of cloud computers is the ability to vectorize the implementation with fewer RAM constraints, thus, achieving faster run times and better scaling with problem size at the cost of higher memory usage. With the lazy-evaluation system provided by Dask, the computations for all frequencies can be submitted in parallel to the cluster. The results are saved to a cloud storage system, where they can be easily accessed and processed.

The run times achieved with VIRGO are compared with the open-source package Bempp-cl.[13] A performance comparison is drawn between a cloud cluster and a local machine, i.e. a personal computer. An AWS cloud cluster was set with an Intel® Xeon® E7 8880 v3 processor, 128 CPUs, and 4 TB of RAM, while the local computer has an Intel R© Core(TM) i7-8750H processor, 6 CPUs, and 32 GB of RAM.

The data shown in Fig. 3 corresponds to a single-frequency, single-source benchmark on the run time using the different packages. Note that for increasing sample sizes, using a personal computer becomes impractical. As the mesh size increases, VIRGO is still faster than Bempp-cl on the local machine. Nonetheless, a shift from the general trend is noticed in the mesh size identified by the black star symbol. This is due to the lack of RAM on the local machine, which is not enough to store and compute the VIRGO's vectorized implementation. Therefore, the machine's solid-state drive is used to store the arrays, making the computation slower than the Bempp-cl implementation. This behavior is expected since VIRGO was designed to be used with cloud clusters; therefore, it is natural to conclude that if one desires to run larger problems on a personal computer, Bempp-cl is still an excellent option.

Figure 3 establishes the advantages of the cloud approach. Considering the multi-frequency and multi-source nature of the problem at hand, it is clear that as more frequencies and sources are desired, one can expect to wait multiple hours or days to obtain the BEM result for a given sample on a personal computer.
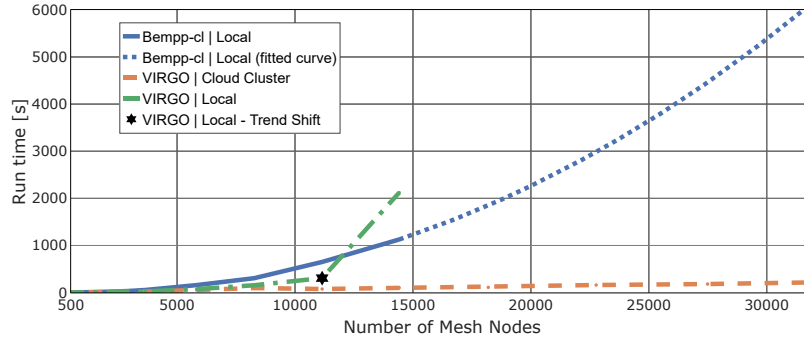
Figure 3: 3D BEM run time benchmark for increasing mesh sizes.

ii.   Simulation Setup

The simulations described follow the ISO 17497-2[2] when considering the source positions to be analyzed. That is 13 sources in the far-field and angular positions described in Table 1.

Position Number	1	2	3	4	5	6	7	8	9	10	11	12	13
Elevation [θ]	0	30	30	30	30	30	30	60	60	60	60	60	60
Azimuth [ϕ]	-	0	60	120	180	240	300	0	60	120	180	240	300

Table 1: Source positions for the 3D goniometer setup.

Receiver positions in the standard regarding the 3D goniometer consider a rotating arc of microphones, which is a practical approach for the measurement given the experimental limitations. With the freedom provided by the numerical method, an idealized receiver distribution is chosen, establishing equal-area coverage on the surface of a hemisphere for every receiver position. Here a high-resolution grid of 4295 receivers is considered with an average θ and ϕ spacing of $1.6°$. This approach allows for smooth visualizations of the 3D polar response, as shown in Fig. 9.

The diffusion coefficient calculation requires third-octave polar responses. Given that a frequency domain method is being used, calculations are done in $\frac{1}{6}$ octave frequency bands and averaged to $\frac{1}{3}$ octave. Simulations are restricted to rigid samples for the current investigation; henceforth, $\beta = 0$ for Eq. (4). The sound sources and receivers are $100\,\text{m}$ and $50\,\text{m}$, respectively from the diffusor.

As described in Section 3.2, the CHIEF formulation is being used to tackle the irregular frequency problem. The internal points, displayed in Fig. 4, are chosen by creating a finite element mesh that discretizes the internal volume with 4-node tetrahedra. The vertices of this new mesh, excluding the boundary elements, are then randomly sampled with the required number of CHIEF points.
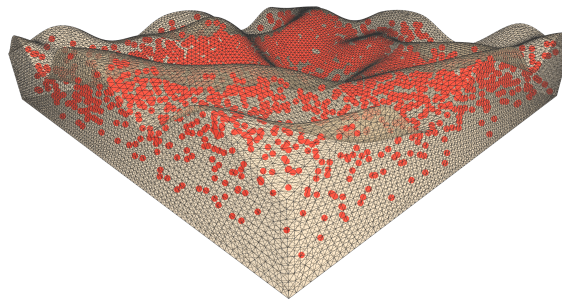

Figure 4: Mesh and CHIEF points for the RPG Waveform Bicubic G.

C.   EXPERIMENTAL SETUP

The 2D goniometer measurement is done on a 1:5 scale. Sound sources are at 2.11 m (10.55 m in 1:1 scale) from the diffusor, and the microphones are placed in a 1.45 m (7.25 m in 1:1 scale) radius arc. The sample is placed at the origin of the system of coordinates, and the incident angles of 0, 30 and 60 degrees are considered.

This measurement was done with a 1:5 scale version of the 30 cm radius hemicylinder and 1 unit of the RPG Modffusor, as shown in Fig. 5. The post-processing steps to extract the diffusion coefficient from the measured impulse responses follow the procedures in ISO 17497-2[2].
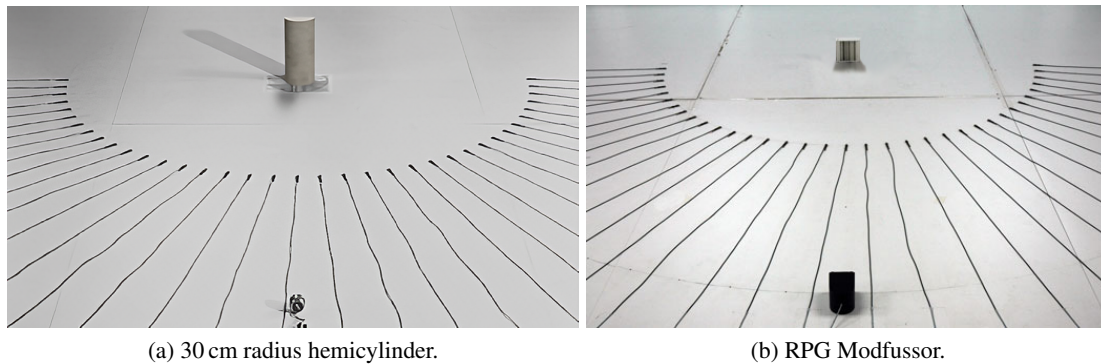

(a) 30 cm radius hemicylinder.   (b) RPG Modfussor.

Figure 5: 2D Goniometer experimental measurement setups.

4.   RESULTS

This section describes and analyses the results achieved from the 3D BEM computations. At first, the hemicylinder and the RPG Modffusor, described in Section 3.1, are simulated, and the results are compared with the experimental measurements of the 2D goniometer, as described in Section 3.3. Then, simulations for the hemisphere and its periodic arrangements are presented, and characteristics of the polar responses are compared with theoretical analyses of periodic samples. Furthermore, the RPG Waveform Bicubic G, which cannot be measured in a 2D goniometer, is simulated with the 3D goniometer setup.

The predictions presented in this section were computed with the cloud cluster described in Section 3.2.1. The total simulation time for all analysis frequencies is presented, considering the diffuser and the reference reflector. It is worth noting that the run time does not include the time taken to initialize the cluster, typically between 2-5 minutes.

A.   COMPARISON WITH EXPERIMENTAL MEASUREMENTS

i.   Hemicylinder

The hemicylinder's normalized diffusion coefficient and scattered polar responses are shown in Fig. 6. The experimental measurement is displayed with the dotted red line, and the numerical simulation is shown in solid blue. Figures 6a and 6b present normalized diffusion coefficient data for normal and random incidence, respectively. Excellent agreement is established between experimental data and the BEM prediction. The most significant deviation is found at 160 Hz in the random incidence normalized diffusion coefficient in Fig. 6b, a difference of 0.098 between measurement and simulation. Additionally, Figs. 6c, 6d and 6e show the angle-dependent diffusion coefficients for the diffusor and the reference reflector. It becomes evident that significant deviations are only found at the lowest analysis frequencies, which is expected given the

increasing experimental uncertainty at this frequency range. Figures 6f, 6g and 6h present polar response comparisons and further reinforces the accuracy of the prediction.

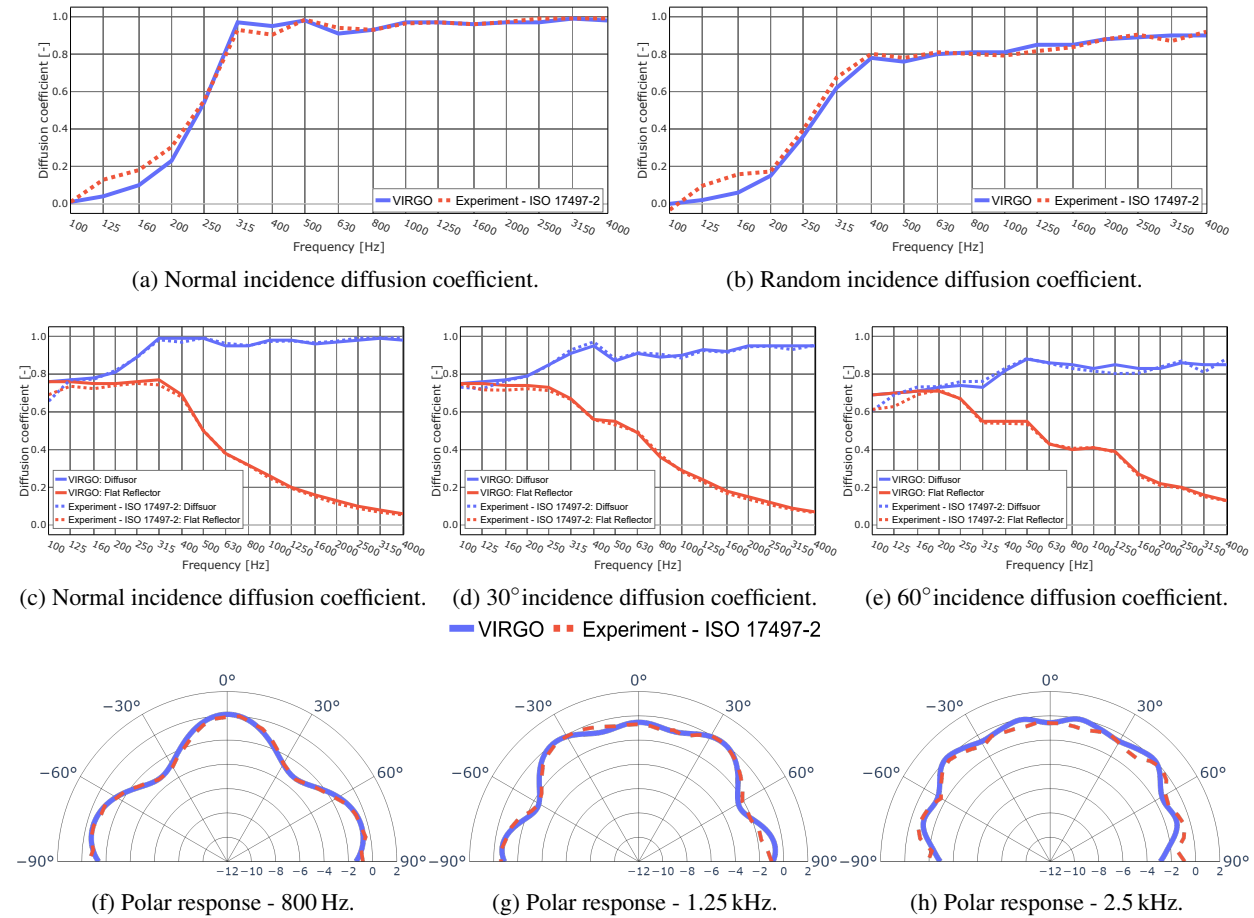The total computation time for the data presented in this section was 14.5 min.

(a) Normal incidence diffusion coefficient.

(b) Random incidence diffusion coefficient.

(c) Normal incidence diffusion coefficient.

(d) 30°incidence diffusion coefficient.

(e) 60°incidence diffusion coefficient.

(f) Polar response - 800 Hz.

(g) Polar response - 1.25 kHz.

(h) Polar response - 2.5 kHz.

Figure 6: Comparison between simulated and measured diffusion coefficients and scattered polar responses for the 30cm radius hemicylinder.

ii.   RPG Modffusor

The diffusion coefficients and scattered polar responses of the Modffusor are shown in Fig. 7. The dotted red line denotes the experimental measurement, and the numerical simulation is shown in solid blue. Figures 7a and 7b present the normalized diffusion coefficient compared to the experimental data (normal and random incidence). The agreement is satisfactory, while the most significant differences are now observed in the random incidence normalized diffusion coefficient at 125 Hz and 630 Hz, with differences of 0.20 and 0.23, respectively.

Additionally, Figs. 7c, 7d and 7e shows the angle-dependent diffusion coefficients for the diffusor and the reference reflector. Here the deviation at 630 Hz becomes evident when looking at the diffusor's diffusion coefficient for 30°incidence and the reference reflector diffusion coefficient for 60°. The error accumulates when normalizing and averaging the results for the random incidence data. At last, normal incidence polar responses are compared with the experiment in Figs. 7f, 7g and 7h. Observing the polar responses makes it clear that the simulation captures the physical phenomena, despite local deviations. The total computation

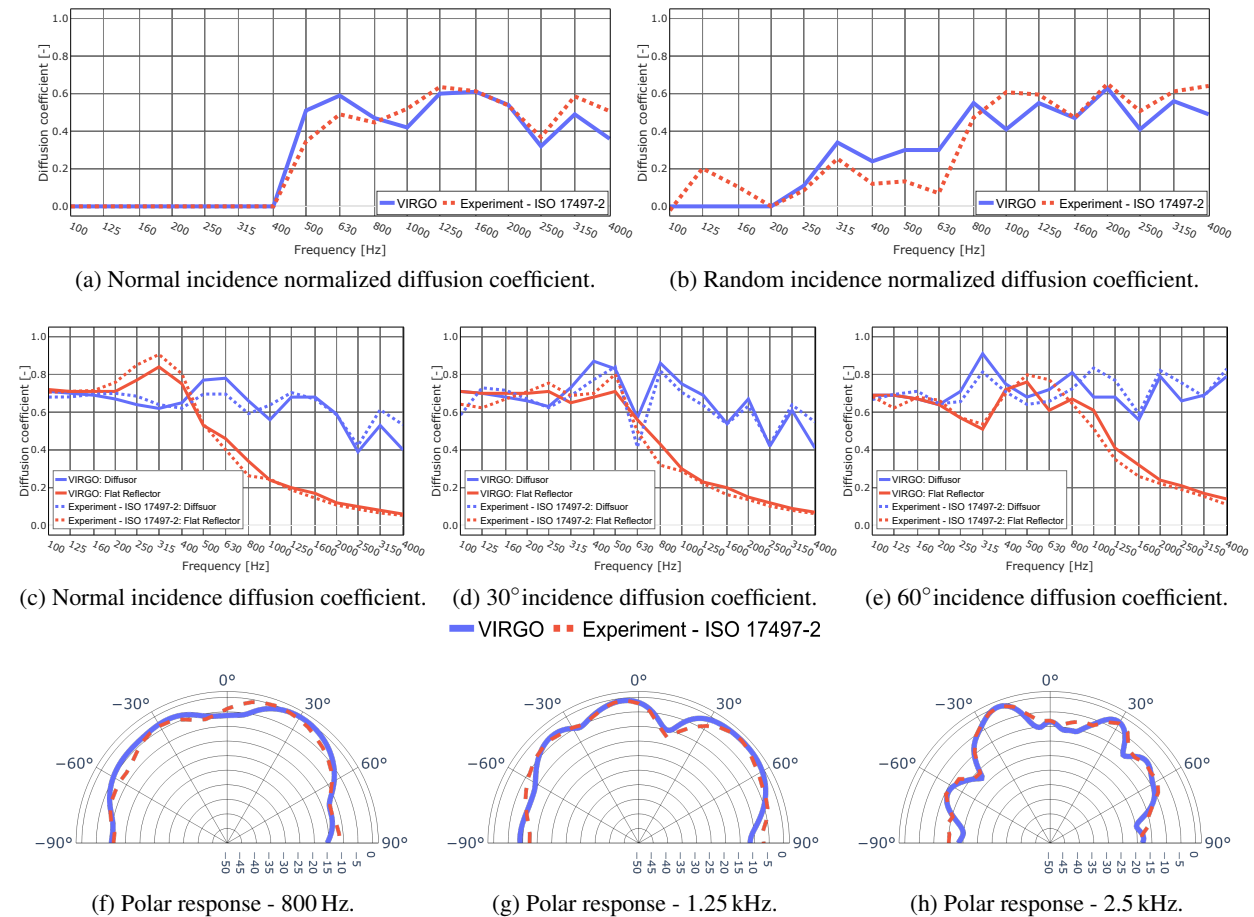time for the data presented in this section was 25.84 min.

(a) Normal incidence normalized diffusion coefficient.

(b) Random incidence normalized diffusion coefficient.

(c) Normal incidence diffusion coefficient.

(d) 30° incidence diffusion coefficient.

(e) 60° incidence diffusion coefficient.

(f) Polar response - 800 Hz.

(g) Polar response - 1.25 kHz.

(h) Polar response - 2.5 kHz.

Figure 7: Comparison between simulated and measured diffusion coefficients and scattered polar responses for the RPG Modffusor.

B.   HEMISPHERE PERIODICITY

When diffusors are arranged in a periodic array, grating lobes will be caused by spatial aliasing in certain directions. These are directions where the path length difference from the source to the receiver via parts of the panel exactly one period apart is an exact multiple of a wavelength.[14] This degrades the polar response, thus lowering the diffusion coefficient of periodic arrays, as illustrated in Fig. 8a.

For a hemisphere, the angles of the grating lobes in the far field can be found analytically with $\sin(\theta) = \frac{m\lambda}{w} - \sin(\phi)$ for any integer $m \in \mathbb{N}$ representing the lobe order and w the sample width. Considering a 60 cm diameter hemisphere, the analytical angles θ_a of the grating lobes for $m = 0, 1, 2, 3$ are $\theta_a = 0°, 15.2°, 31.6°, 51.8°$. Figure 8b shows the polar response of the simulated array of 4x1 hemispheres, with simulated grating lobes $\theta_s = 0°, 14.7°, 31.3°, 51.2°$. The difference is acceptable to validate the numerical approach. The frequency of 2113 Hz was chosen to better visualize the grating lobes.

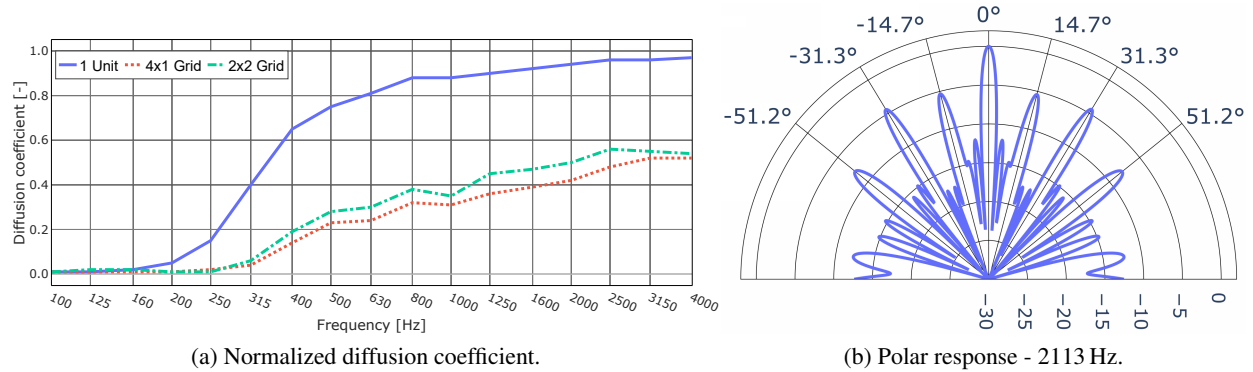(a) Normalized diffusion coefficient.

(b) Polar response - 2113 Hz.

Figure 8: Left: comparison between normalized diffusion coefficient for a single hemisphere, a 4x1 grid, and a 2x2 grid. Right: polar response for 4x1 hemisphere arrangement at 2113 Hz.

With the proposed method, the periodicity effect can also be visualized in 3D. Figure 9 shows a top view of the 3D polar responses at 400 Hz and 2.5 kHz for the four hemisphere configurations described in Section 3.1. Even at lower frequencies, the grating lobes can be easily observed when comparing Figs. 9a and 9b. This effect is extended in two directions when the 2x2 array is considered, as shown in Fig. 9c. As the frequency increases, the effect is even more prominent, as depicted by the comparison between Fig. 9d, and Figs. 9e and 9f. The computation times for the 1x1, 4x1, and 2x2 hemisphere arrangements presented in this section were 2.72 min, 8.12 min, and 8.56 min, respectively.
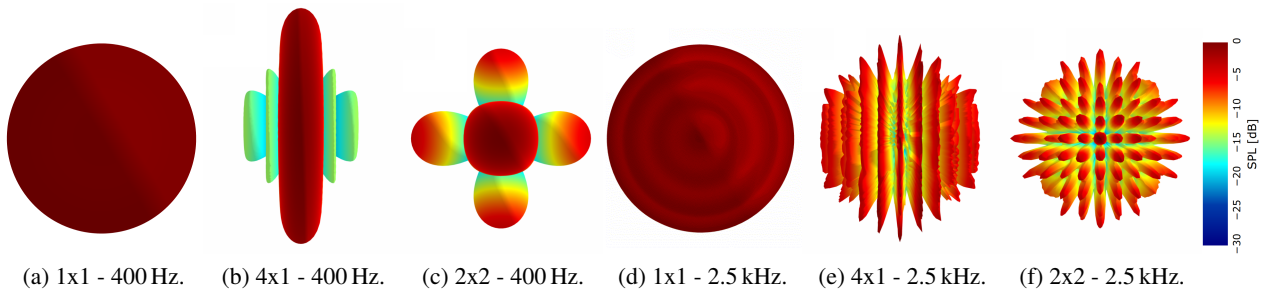

(a) 1x1 - 400 Hz.   (b) 4x1 - 400 Hz.   (c) 2x2 - 400 Hz.   (d) 1x1 - 2.5 kHz.   (e) 4x1 - 2.5 kHz.   (f) 2x2 - 2.5 kHz.

Figure 9: 3D polar response of different arrangements of hemispheres.

C.   RPG WAVEFORM BICUBIC G

As described in Section 3.1, the RPG Waveform Bicubic G is characterized as an example of a 2D diffusor. Since no current measurement is available with a 3D goniometer, only numerical data is presented. The diffusion coefficients for normal and random incidence are shown in Figs. 10a and 10b.

Furthermore, the 3D polar plots for the diffuser, Figs. 10c, 10d, 10e and 10f; and for the reference reflector, Figs. 10g, 10h, 10i and 10j are shown. The specular component of the scattered pressure from the reference reflector becomes increasingly apparent at higher frequencies. The total computation time for the data presented in this section was 21 min.

(a) Normal incidence diffusion coefficient.

(b) Random incidence diffusion coefficient.

(c) 250 Hz.

(d) 500 Hz.

(e) 1 kHz.

(f) 3.15 kHz.
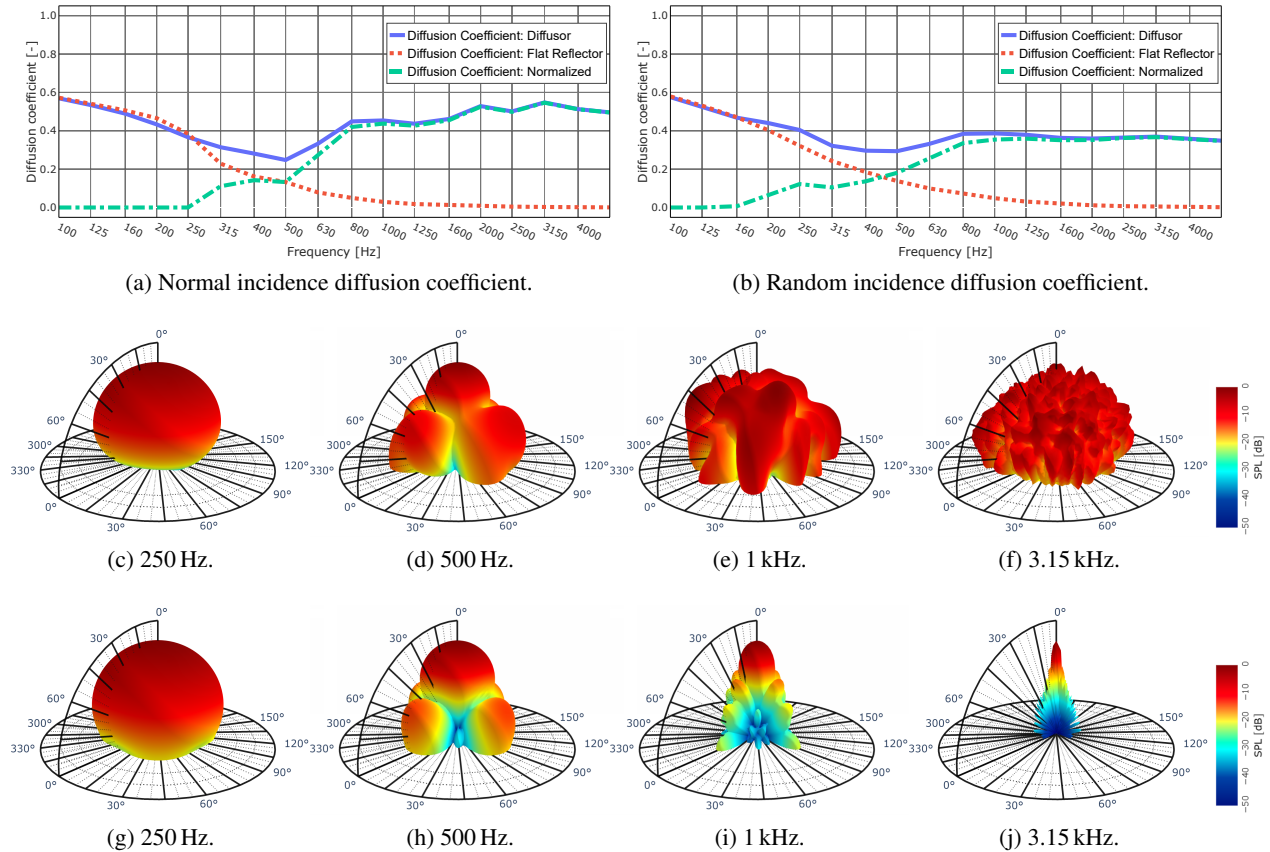
(g) 250 Hz.

(h) 500 Hz.

(i) 1 kHz.

(j) 3.15 kHz.

Figure 10: Diffusor, reference reflector, and normalized diffusion coefficient for random and normal incidence; normal incidence 3D polar response for the RPG Waveform Bicubic G (10c, 10d, 10e and 10f) and the reference reflector (10g, 10h, 10i and 10j)

5. CONCLUSION

The VIRGO framework, based on the 3D BEM, was described and used to compute the diffusion coefficient and 3D polar plots. It was shown that a cloud-based approach is more efficient than simulating on personal computers. Henceforth, following the ISO 17497-2[2] is now possible for various cases, as samples can be computed from 100 Hz to 5 kHz in a reasonable time frame.

Good agreement has been found between the scale measurements in the 2D goniometer and the numerical validations. Evaluating different periodic arrangements of hemispheres produced results that agree with the theoretical grating lobe prediction. At last, a commercial 2D diffusor was computed.

Further research should address the irregular frequencies problem with the more robust Burton-Miller[8] approach. A BEM implementation with discontinuous linear elements must also be considered, as it provides advantages over the current approach.[15] As demonstrated by Martinez,[16] samples with thin sections can also result in a breakdown of Eq. (4). Henceforth a thin-plate formulation would further expand the possible models that can be simulated. Additionally, for larger samples or periodic/modulated arrays, computational resource limitations are still an obstacle to fast computing. New ways of distributing the problem must be developed, allowing larger meshes with > 50000 nodes to be computed efficiently.

The total computational run-time for all six test cases presented in this paper was approximately 81 minutes, costing \$ 15.00. VIRGO's cloud-based numerical approach provides a fast and cheap alternative given the complications and expenses of performing the measurements specified by ISO 17497-2[2].

REFERENCES

[1] T. J. Hargreaves, T. J. Cox, Y. W. Lam, and P. D'Antonio, "Surface diffusion coefficients for room acoustics: Free-field measures," *The Journal of the Acoustical Society of America*, vol. 108, no. 4, pp. 1710–1720, 2000.

[2] ISO 17497-2:2012, "Acoustics — sound-scattering properties of surfaces — part 2: Measurement of the directional diffusion coefficient in a free field."

[3] T. J. Cox and Y. Lam, "Prediction and evaluation of the scattering from quadratic residue diffusers," *The Journal of the Acoustical Society of America*, vol. 95, no. 1, pp. 297–305, 1994.

[4] J. Hargreaves and T. Cox, "A transient boundary element method model of Schroeder diffuser scattering using well mouth impedance.," *The Journal of the Acoustical Society of America*, vol. 124, no. 5, p. 2942, 2008.

[5] M. Vorländer and E. Mommertz, "Definition and measurement of random-incidence scattering coefficients," *Applied acoustics*, vol. 60, no. 2, pp. 187 – 199, 2000.

[6] C. Geuzaine and J.-F. Remacle, "Gmsh: A 3-d finite element mesh generator with built-in pre- and post-processing facilities," *International Journal for Numerical Methods in Engineering*, vol. 79, pp. 1309 – 1331, September 2009.

[7] S. Marburg and B. Nolte, *Computational Acoustics of Noise Propagation in Fluids - Finite and Boundary Element Methods*. Springer Berlin Heidelberg, 2008.

[8] A. J. Burton and G. F. Miller, "The Application of Integral Equation Methods to the Numerical Solution of Some Exterior Boundary-Value Problems," *Proceedings of the Royal Society of London Series A*, vol. 323, pp. 201–210, June 1971.

[9] S. Marburg and S. Amini, "Cat's eye radiation with boundary elements: Comparative study on treatment of irregular frequencies," *Journal of Computational Acoustics*, vol. 13, 03 2005.

[10] T. WU, *Boundary Element Acoustics: Fundamentals and Computer Codes*. WIT Press / Computational Mechanics (September 6, 2000), 2000.

[11] N. Atalla and F. Sgard, *Finite Element and Boundary Methods in Structural Acoustics and Vibration*. CRC Press, 2015.

[12] Dask Development Team, *Dask: Library for dynamic task scheduling*, 2016.

[13] T. Betcke and M. W. Scroggs, "Bempp-cl: A fast Python based just-in-time compiling boundary element library," vol. 6, no. 59, p. 2879, 2021.

[14] T. Cox and P. D'Antonio, *Acoustic Absorbers and Diffusers, Third Edition: Theory, Design and Application*. CRC Press, 2016.

[15] S. Marburg and S. Schneider, "Influence of element types on numeric error for acoustic boundary elements," *Journal of Computational Acoustics*, vol. 11, pp. 363–386, 09 2003.

[16] R. Martinez, "The thin-shape breakdown (tsb) of the helmholtz integral equation," *The Journal of the Acoustical Society of America*, vol. 90, no. 5, pp. 2728–2738, 1991.